

Article

Reduced Graphene Oxide/ZnIn₂S₄ Nanocomposite Photocatalyst with Enhanced Photocatalytic Performance for the Degradation of Naproxen under Visible Light Irradiation

Kun Fu ^{1,2}, Yishuai Pan ^{1,2}, Chao Ding ^{1,2}, Jun Shi ^{1,2,3,*} and Huiping Deng ^{1,2,3,*}

¹ Key Laboratory of Yangtze River Water Environment, Ministry of Education, Shanghai 200092, China; fukun@tongji.edu.cn (K.F.); panyishuai@tongji.edu.cn (Y.P.); dc_knight@outlook.com (C.D.)

² College of Environmental Science and Engineering, Tongji University, Shanghai 200092, China

³ Shanghai Institute of Pollution Control and Ecological Security, Shanghai 200092, China

* Correspondence: shijun215@tongji.edu.cn (J.S.); denghuiping@tongji.edu.cn (H.D.)

Received: 4 June 2020; Accepted: 22 June 2020; Published: 24 June 2020



Abstract: The development of photocatalysts with visible light response is of great significance to cope with energy crisis and environmental remediation. In this study, a visible light-driven photocatalyst reduced graphene oxide/ZnIn₂S₄ (rGO/ZIS) was prepared by a facile one-pot hydrothermal method. The photocatalyst was used for the degradation of naproxen under visible light illumination and it exhibited remarkably degradation efficiency (nearly 99% within 60 min). The improved photocatalytic degradation performance can be attributed to the enhancement of light adsorption capacity and effective separation of photoinduced electron–hole pairs. The reactive species quenching experiments and EPR measurements demonstrated that superoxide radical ($\bullet\text{O}_2^-$) and hole (h^+) play a dominant role in the photocatalytic degradation reactions. In addition, the degradation intermediates were identified and the degradation pathway was suggested.

Keywords: ZnIn₂S₄; visible light; photocatalyst; degradation; naproxen

1. Introduction

Over the last few decades, pharmaceuticals and personal care products (PPCPs)—an emerging class of refractory organic pollutants—have been ubiquitously detected in wastewater treatment plant effluents, surface water, ground water, and even some drinking water [1]. It has become a serious environmental and human health concern because of the potential risks posed by PPCPs which include acute and chronic toxicity, the occurrence of antibiotic resistance genes, etc. [2]. Naproxen (NPX), as one of representative nonsteroidal anti-inflammatory drug (NSAID), has been widely used in the treatment of rheumatoid arthritis due to its analgesic and antipyretic properties [3,4]. It has been frequently detected in various water environment, and its concentration ranges from ng/L to $\mu\text{g/L}$. Although the concentration of NPX is relatively low, long-term accumulation and enrichment in water and soil will have a serious impact on aquatic organisms and ecosystem [5]. In addition, some researchers have found that people who ingest trace NPX have a higher risk of heart attack or bladder cancer [6,7]. However conventional water and waste treatment processes are insufficient for the removal of NPX. Therefore, highly effective treatment methods for the elimination of NPX are urgently needed to develop.

Among different approaches for the removal of PPCPs, Photocatalytic degradation has become a promising method by virtue of its high efficiency and energy-saving. However, the traditional photocatalyst (such as TiO₂ and ZnO) with wide band gap can only exploit ultraviolet region

light which accounts for only 4% of the total solar spectrum, thus greatly restricts their practical applications [8]. Therefore, in order to make full use of solar energy, it is necessary to develop visible light driven photocatalysts.

Recently, ZnIn_2S_4 , as an important 2D layered ternary chalcogenide semiconductor, has attracted increasing attention because of its unique electronic and optical characteristics [8,9]. After Lei's group synthesized visible-light-driven photocatalyst ZnIn_2S_4 in 2003, researches regarding ternary metal chalcogenide ZnIn_2S_4 are increasingly reported [10]. It has been a promising photocatalyst used in contaminants degradation [11–13], hydrogen evolution [14–16], and CO_2 reduction [17] due to its appropriate band edges, eco-friendly property, excellent photoactivity, as well as chemical stability. Reduced graphene oxide (rGO), a two-dimensional (2D) sp^2 carbon allotrope, has attracted a wide range of interests owing to its outstanding features such as large theoretical specific surface area, good electrical conductivity as well as excellent chemical stability [18]. The high electron conductivity can hinder the recombination of photoinduced electron–hole pairs, thus improving photocatalytic activity.

Therefore, the combination of ZnIn_2S_4 and RGO is expected to further improve the photocatalytic performance of ZnIn_2S_4 . On one hand, RGO can act as a good catalyst support, on the other hand, it can be used as a favorable acceptor and mediator of photogenerated electrons [19]. Most of studies have demonstrated that the addition of RGO can improve the performance of composite photocatalysts [19–22]. Xie et al. synthesized nano-sized rGO/ CuInS_2 photocatalyst via a simple one-step solvothermal method [21]. The results demonstrated that the photocatalytic efficiency of the rGO/ CuInS_2 was far superior to that of pure rGO/ CuInS_2 for the 2-nitrophenol removal. Li et al. synthesized graphene coated ZnIn_2S_4 microspheres—with enhanced interfacial contact [22]. The results shown that the large interfacial area and speedy charge carriers transfer route are of great significance for the heterojunction materials to facilitate photoinduced charge separation.

Herein, we synthesized reduced GO/ ZnIn_2S_4 (rGO/ZIS) nanocomposite photocatalyst by a simple one-step hydrothermal method. The morphologies and optical-electrical properties were characterized. The photocatalytic activities of rGO/ZIS was evaluated by photocatalytic degradation of naproxen under visible light. In addition, the degradation intermediates were identified by LC/MS/MS, the possible degradation pathway was proposed and the degradation mechanism was elucidated.

2. Results and Discussion

2.1. Characterization

The morphology and microstructure of the composites were studied by SEM and TEM. As can be seen in Figure 1a, pure ZnIn_2S_4 shows an irregular morphology formed by self-assembly of sheet structure, while homogeneous spherical particles were observed in rGO/ZIS-1 (Figure 1b,c), which is probably because the addition of GO enables ZnIn_2S_4 to be fixed on its surface and self-assembled uniformly in all directions. Furthermore, Figure 1d–f shows the HRTEM of rGO/ZIS-1, which exhibits a nanoscale layered structure, the interplanar distances of 0.33 nm should be assigned to the (101) plane of ZnIn_2S_4 . The microstructure and compositional distribution of the composite photocatalyst were further investigated by EDS mapping. The EDS elemental mapping (Figure 1g) clearly revealed that the elements of S, In, and Zn were uniformly distributed in a spherical particle located in the center of analyzed area, however C and O elements were homogeneously scattered in the surrounding space, confirming the successful combination of ZnIn_2S_4 and graphene oxide.

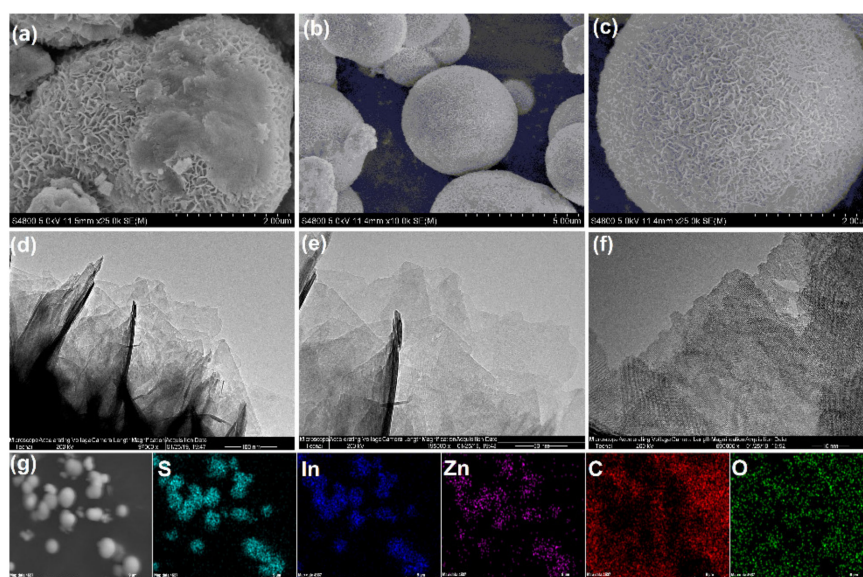


Figure 1. SEM images of ZnIn_2S_4 (a) and rGO/ZIS-1 (b,c); TEM images of rGO/ZIS-1 with different magnification (d–f); TEM image of rGO/ZIS-1 and corresponding energy-dispersive X-ray spectroscopy (EDS) elemental mapping for S, In, Zn, C, and O (g).

The XRD patterns of as-prepared samples were investigated and shown in Figure 2a. For the pure ZnIn_2S_4 , all the characteristic peaks could be indexed to a hexagonal phase of ZnIn_2S_4 (JCPDS no. 65–2023) [8]. Graphene oxide (GO) shows a characteristic peak at $2\theta = 10.8^\circ$ and a weak peak at $2\theta = 42^\circ$, which can be ascribed to the (002) and (100) planes respectively [23], however, no obvious diffraction peak of GO was observed in rGO/ZIS, indicating the reduction and/or pyrolysis of GO during the hydrothermal reaction [23,24]. The peak positions of rGO/ZIS stay unchanged, implying that the incorporation of GO in the composite hardly alter the crystal phase of rGO/ZIS, which may due to the high dispersion or low content of rGO [21]. In addition, however, the FT-IR spectra can further confirm the existence of RGO in the nanocomposite, as shown in Figure 2b. The peak at 1048 , 1250 , and 1727 cm^{-1} displayed in GO can be ascribed to the stretching vibration bands of oxygen-containing functional groups including C–O, C–OH, and C=O [25]. for ZnIn_2S_4 , two peaks at 1619 and 1396 cm^{-1} are attributed to the water molecules and hydroxyl groups absorbed on surface [18]. rGO/ZIS nanocomposites show peaks at 1048 and 1620 cm^{-1} corresponding to the C–O stretching vibrations and skeletal vibration, respectively. the intensity of some peaks weakened or disappeared in the FT-IR spectrum of ZIS/rGO further indicating the partial reduction of graphene oxide to rGO.

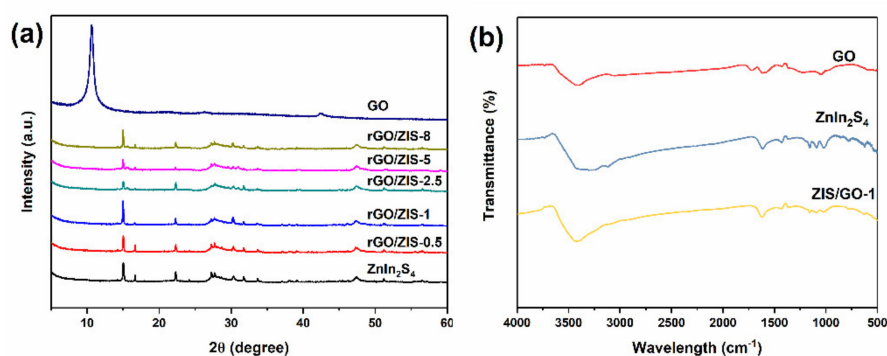


Figure 2. (a) XRD patterns and (b) FT-IR spectra of the as-prepared samples.

The analysis of chemical composition and corresponding valence states in composite was carried out using XPS measurements (Figure 3). Figure 3a shows the XPS spectra for a survey scan of rGO/ZIS-1,

the result demonstrated that the main elements of the composite are Zn, In, S, C, and O, respectively. The peaks shown in Figure 3b centered at 1022.18 and 1045.32 eV can be ascribed to Zn 2p_{3/2} and Zn 2p_{1/2}. The two symmetric peaks at 452.56 eV and 445 eV were assigned to In 3d_{3/2} and In 3d_{5/2}, respectively [8].

In addition, the binding energies of S 2p_{3/2} and S 2p_{1/2} in Figure 3c are located at 161.67 eV and 162.87 eV, respectively, which is associated with S²⁻ in the composite [26]. Figure 3e shows the high-resolution spectrum of C 1s in rGO/ZIS-1, the binding energy at 284.6, 286.5, 287.5, and 289 eV were corresponding to C=C/C-C, C-O, C=O, and O-C=O, respectively [27]. Compared with GO (Figure S1), the intensity of oxygen containing functional groups in rGO/ZIS-1 is significantly reduced, indicating that the GO was partially reduced to rGO during the hydrothermal reaction. In addition, Figure S2 and Table S1 displayed the results of N₂ adsorption-desorption isotherm and BJH pore size distribution of as-prepared samples. All the samples showed a type IV isotherm and a H3 hysteresis loop, which indicated that the pores in composites are mainly formed by self-assembly of slit-like lamellar structures. Compared with GO and ZnIn₂S₄, the specific surface area and pore volume of rGO/ZIS-1 were improved, which facilitated the adsorption and degradation of pollutants by providing more surface-active sites.

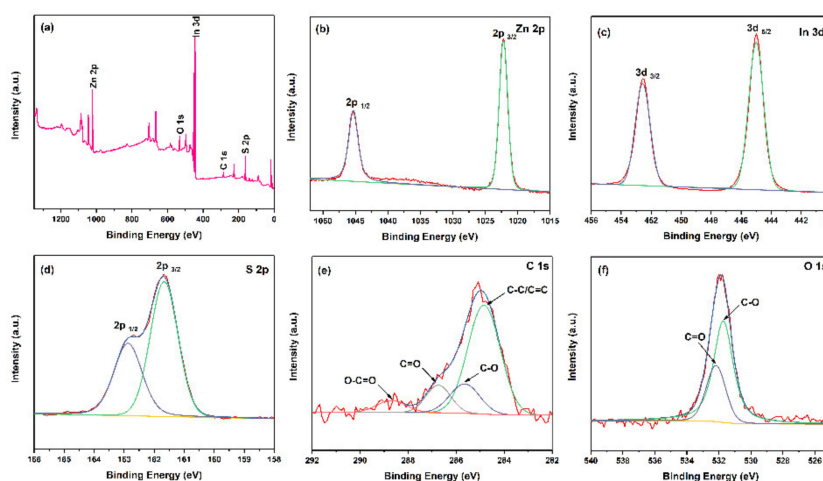


Figure 3. XPS spectra of the GO/ZIS-1. (a) Survey of the sample, (b) Zn 2p, (c) In 3d, (d) S 2p, (e) C 1s, (f) O 1s.

The optical properties of the as-prepared samples was studied by the UV-vis DRS analysis, and the results were shown in Figure 4a. ZnIn₂S₄ had a high absorbance in the whole UV-vis light spectrum, and the absorbance edge is around 700 nm. The light absorbance of rGO/ZIS-1 enhanced as compared with ZnIn₂S₄. Furthermore, the band gap energy (E_g) of the samples can be estimated using the equation

$$\alpha h\nu = A(h\nu - E_g)^{n/2} \quad (1)$$

where α , h , ν , A , and E_g represents the absorption coefficient, Planck constant, light frequency, proportional constant and band gap energy, respectively. The $(\alpha h\nu)^2$ vs. $h\nu$ -profiles for GO, ZnIn₂S₄ and rGO/ZIS-1 were depicted in Figure 4b. The band gap energy of samples is determined by extrapolation method when $(\alpha h\nu)^2$ is equal to 0. The values of band gap energy of ZnIn₂S₄ and rGO/ZIS-1 is calculated to be 1.93 eV and 1.88 eV. Compared with the energy band of ZnIn₂S₄, the energy band of rGO/ZIS-1 is slightly narrowed, which indicated that the presence of GO does not significantly affect the energy band structure of ZnIn₂S₄. The valance band (VB) and conduction band (CB) edge potential of rGO/ZIS-1 can be determined by the equation

$$E_{VB} = X - E^e + 0.5E_g \quad (2)$$

where E_{VB} is VB edge potential, X , E^e , and E_g represents Mulliken's electronegativity, the energy of free electrons on the hydrogen scale (~ 4.5 eV) and band gap energy, respectively [28]. The X value of pure $ZnIn_2S_4$ is estimated to be about 4.86, thus the E_{VB} and E_{CB} were calculated to be +1.3 and -0.58 eV, respectively. PL analysis was further carried out to study the recombination rate of the photogenerated electron and holes. Figure 4c shows the PL emission intensities of as-prepared samples centered at around 465 nm, which is in the order of $ZnIn_2S_4 > rGO/ZIS-1 > GO$. It is well known that the stronger the PL emission intensity is, the higher the recombination rate and possibility of the photogenerated carriers are [29]. The emission intensity of rGO/ZIS-1 reduced evidently when compared with $ZnIn_2S_4$, indicating that the incorporation of GO into the $ZnIn_2S_4$ clearly inhibit the recombination rate of photogenerated electron-hole pairs, and thus enhance the photocatalytic performance. In addition, the interface charge separation efficiency was measured by electrochemical impedance spectra (EIS). In general, the smaller curvature diameter of the EIS Nyquist plot means the smaller interfacial electron transfer resistance [8]. It can be seen in Figure 4d that the curvature diameter of rGO/ZIS-1 is smaller than $ZnIn_2S_4$, which suggested that the rGO/ZIS-1 could improve the photocatalytic activity by reducing the interfacial charge transfer resistance and then facilitating the separation and migration of charges at the interface.

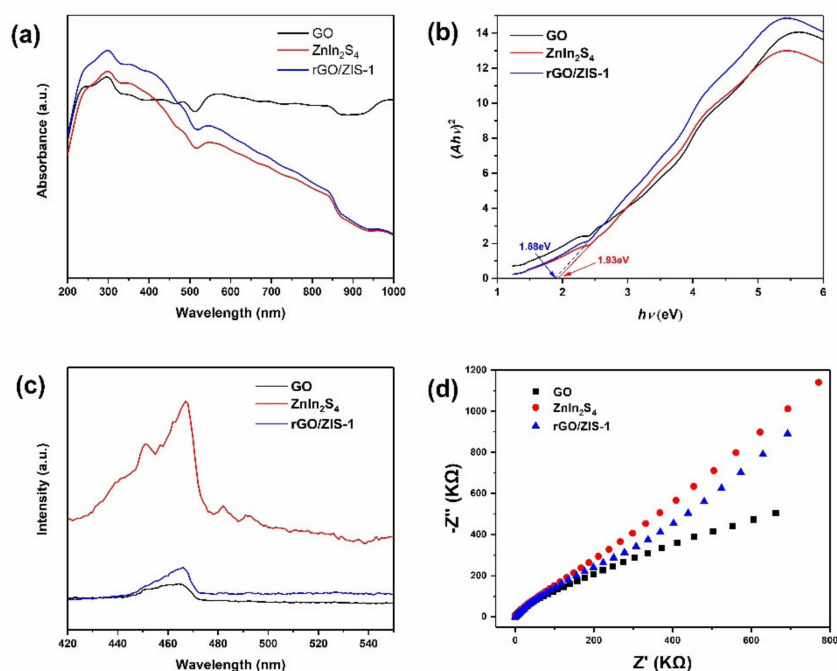


Figure 4. (a) UV-vis diffuse reflectance spectra and the corresponding (b) $\alpha h\nu^2$ versus $h\nu$ curves of the GO, $ZnIn_2S_4$ and rGO/ZIS-1; (c) PL spectra; and (d) EIS Nyquist plots of GO, $ZnIn_2S_4$, and rGO/ZIS-1.

2.2. Photocatalytic Performance

The photocatalytic activities of rGO/ZIS composites were tested by the degradation of NPX under visible light irradiation and the results were displayed in Figure 5 as can be seen from Figure 5a, in the scenario of dark adsorption and self-degradation of NPX, NPX is hardly degraded or removed. Compared with this, all the rGO/ZIS composites showed a remarkable removal efficiency for NPX within 60 min. Furthermore, the photodegradation rate can be calculated by the pseudo first-order kinetic equation

$$\ln(c_t/c_0) = -kt \quad (3)$$

where k represents apparent rate constant, t is the irradiation time, C_0 and C_t are the initial and t time concentration of pollutants. rGO/ZIS-1 demonstrated the fastest degradation rate (99% within 60 min)

and the highest k value than that of other samples. The k value corresponding to the degradation of NPX was 0.082 min^{-1} , about 1.3 times higher than that of ZnIn_2S_4 alone (Figure 5b), which indicated that the introduction of GO made a good contribution to the promotion of NPX degradation efficiency. However, appropriate GO concentration is very important to improve the photocatalytic activity of rGO/ZIS composites. Therefore, rGO/ZIS-1 was chosen as the optimal photocatalyst for the following experiments. As shown in Figure 5c, with the decrease of initial concentration of NPX, the degradation rate of NPX decreased gradually, which is due to the ample active sites and reactive species has a quantitative superiority over NPX with low concentration. By the similar token, the higher concentration of photocatalyst will produce higher concentration of active sites and reactive species, which will accelerate the degradation rate of NPX (Figure 5d).

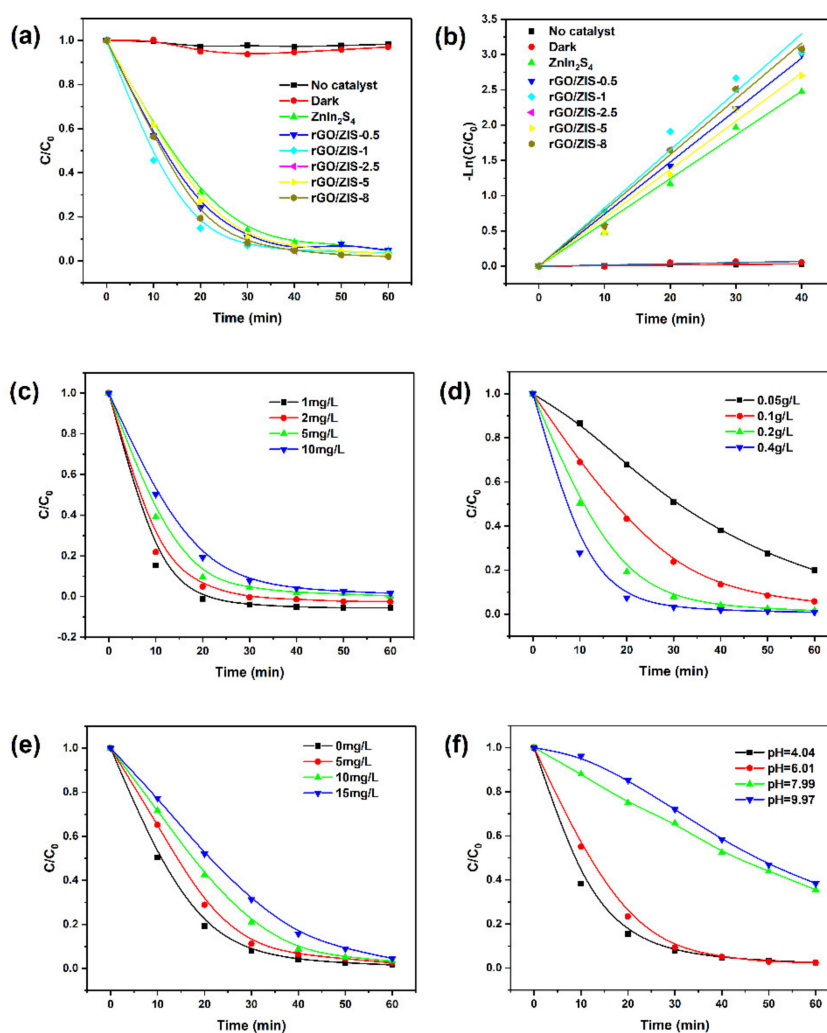


Figure 5. (a) Photocatalytic degradation of NPX with different photocatalysts and (b) plots of $-\ln(C/C_0)$ vs irradiation time; Effects of initial concentration of NPX (c), photocatalyst dosage (d), HA (e) and pH (f) on NPX photodegradation by rGO/ZIS-1. Reaction conditions: $[\text{NPX}] = 10 \text{ mg}\cdot\text{L}^{-1}$, $[\text{photocatalyst}] = 0.2 \text{ g}\cdot\text{L}^{-1}$, natural pH for (a), (b), (c), (d), and (e), $\lambda > 420 \text{ nm}$.

Because of the widespread existence of natural organic matter (NOM) in environmental water, it will affect the photocatalytic degradation to a certain extent. As a major constitute of NOM, the effect of humic acid (HA) with different concentration on the photodegradation of NPX was investigated. It can be seen from Figure 5e, the degradation rate of NPX decreased gradually with the increase of HA concentration, On the one hand, it can be attributed to the competitive effect of HA on reactive

species, on the other hand, it may be due to the shielding effect of HA on irradiation light. It is well known that pH not only affects the surface charges of catalyst and ionization of organic compounds, but also influences their interactions. Therefore, the effect of initial pH ($pH_{ini} = 4.04, 6.01, 7.99,$ and 9.97) on the photocatalytic degradation performance of NPX was carried out. The pK_a value of NPX is 4.15, thus NPX existed as a neutral molecule when $pH < 4.15$ and deprotonated to anionic form NPX^- when $pH > 4.15$. The measured isoelectric point of rGO/ZIS-1 was about 6.95 (Figure S3), hence when $pH > 6.95$, the electrostatic repulsion between negatively charged surface of rGO/ZIS-1 and NPX^- prevented them from approaching each other, resulting in the reduction of degradation rate. In addition, rGO/ZIS-1 was used for the removal of diclofenac to testify its universality and the results were shown in Figure S4. rGO/ZIS-1 exhibited the best photocatalytic performance than that of other as-prepared photocatalysts and the removal efficiency reached 99.4% within 60 min. The rate constant k is 5.6 times higher than that of pure $ZnIn_2S_4$.

2.3. Photocatalytic Mechanism

Generally, hydroxyl radical ($\bullet OH$), superoxide radical ($\bullet O_2^-$) and hole (h^+) are the main three reactive species that are responsible for the photocatalytic degradation of organic pollutants. In order to estimate their contribution during the photocatalytic process of NPX, the reactive species quenching experiments were carried out using different scavengers. As shown in Figure 6a, ethylenediamine tetra acetic acid disodium salt (EDTA-2Na, 1.0 mM), isopropanol (IPA, 1.0 mM), *p*-benzoquinone (BQ, 1.0 mM), and furfuryl alcohol (FFA, 1.0 mM) were chosen as the scavengers for h^+ , $\bullet OH$, $\bullet O_2^-$, and 1O_2 respectively. No obvious effect on the NPX photodegradation efficiency was observed when the IPA and FFA were added as quenching agents respectively, suggesting the $\bullet OH$ and 1O_2 were not the dominant reactive species in the experiments of NPX-photodegradation. However, the removal of NPX was greatly inhibited in the presence of EDTA-2Na or BQ, and the NPX degradation efficiency decreases from 96.44% to 35.46% and 60.19%, respectively (Figure 6b). Which indicated that the h^+ and $\bullet O_2^-$ might play the key roles in the NPX photocatalytic degradation process. To further affirm the above results, EPR measurements were conducted to in situ determine the $\bullet OH$ and $\bullet O_2^-$ radicals produced on the photocatalysts surface as the results shown in Figure 6c, no EPR signal was detected in the absence of light irradiation. By comparison, when the light is on, both $ZnIn_2S_4$ and rGO/ZIS-1 exhibited typical 1:1:1:1 spectra of DMPO- $\bullet O_2^-$ adducts, and the signal of rGO/ZIS-1 is stronger than that of $ZnIn_2S_4$, implying the enhancement of $\bullet O_2^-$ generation. However, no signal of DMPO- $\bullet OH$ adducts was observed, indicating the absence of $\bullet OH$ during the NPX degradation process, which is consistent with the reactive species quenching experiments in Figure 6a based on the above results, h^+ and $\bullet O_2^-$ were the two main reactive species that contributed to the NPX photocatalytic degradation, the effect of $\bullet OH$ and 1O_2 were negligible.

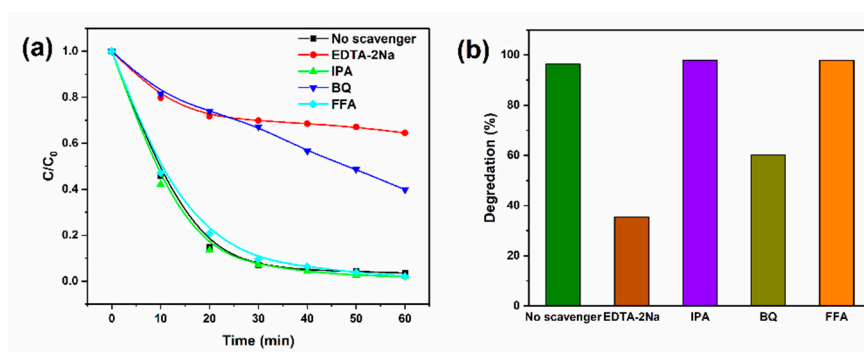


Figure 6. Cont.

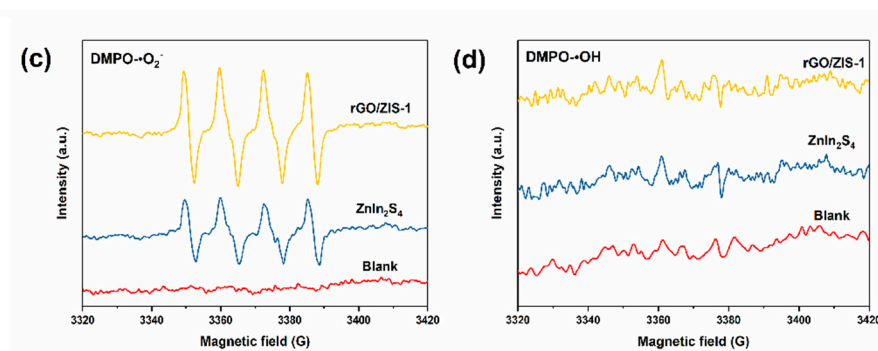
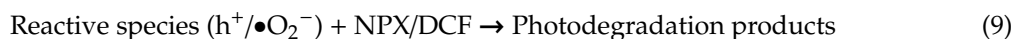
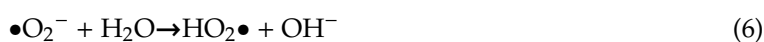


Figure 6. (a) NPX photodegradation over rGO/ZIS-1 and (b) corresponding degradation efficiency in the presence of 1.0 mM various scavengers; (c) EPR spectra of DMPO- $\bullet\text{O}_2^-$ and (d) DMPO- $\bullet\text{OH}$ adducts over different photocatalysts with irradiation for 5 min. Reaction conditions: $[\text{NPX}] = 10 \text{ mg}\cdot\text{L}^{-1}$, $[\text{photocatalyst}] = 0.2 \text{ g}\cdot\text{L}^{-1}$, $[\text{DMPO}] = 100 \text{ mM}$, natural pH, $\lambda > 420 \text{ nm}$.

Despite the main reactive species contributed to the photodegradation of NPX have been identified, it is still of significance to study the underlying generation and transfer route of photoinduced electron-hole pairs. Based on above experiment results and established energy band structure, the possible transfer route of photogenerated carriers and photocatalytic mechanism were determined and shown in Figure 7. ZnIn_2S_4 can easily generate electron-hole pairs under the visible light irradiation. The photogenerated electrons on the conduction band (CB) reduce the dissolved oxygen (O_2) absorbed on the surface of photocatalyst to superoxide radical ($\bullet\text{O}_2^-$), because of the CB edge potential (-0.58 eV) is more negative than $E^\theta (\text{O}_2/\bullet\text{O}_2^-)$ (-0.33 V vs. NHE) [30]. However, the photogenerated holes on the valence band (VB) cannot oxidize the $\text{OH}^-/\text{H}_2\text{O}$ into $\bullet\text{OH}$ due to the VB edge potential E_{VB} ($+1.3 \text{ eV}$) is less positive than $E^\theta (\bullet\text{OH}/\text{OH}^-)$, 1.99 eV vs. NHE ; $\bullet\text{OH}/\text{H}_2\text{O}$, 2.27 eV vs. NHE). rGO not only acts as a support, but also serves as a good electron acceptor and transmission medium, which enhanced the effective separation of photogenerated charge carriers. Then, the generated reactive species h^+ and $\bullet\text{O}_2^-$ will directly degrade NPX relying on its strong redox ability. The related reactions can be summed up as below:



2.4. Reusability and Stability

For the sake of evaluating the reusability and stability of photocatalysts, cycling experiments were carried out using rGO/ZIS-1 as photocatalyst under the same conditions and the results were displayed in Figure 8a. After five repeated runs of photocatalytic test, rGO/ZIS-1 still has a degradation efficiency of 96.1% for NPX, which is slightly lower than that of first run (98.4%). Besides, there is no distinct change in the survey XPS spectra after five consecutive cycles (Figure 8b), illustrating that the rGO/ZIS-1 composite photocatalyst has relatively high reusability and stability in the photocatalytic degradation of NPX and DCF, which is beneficial to practical application.

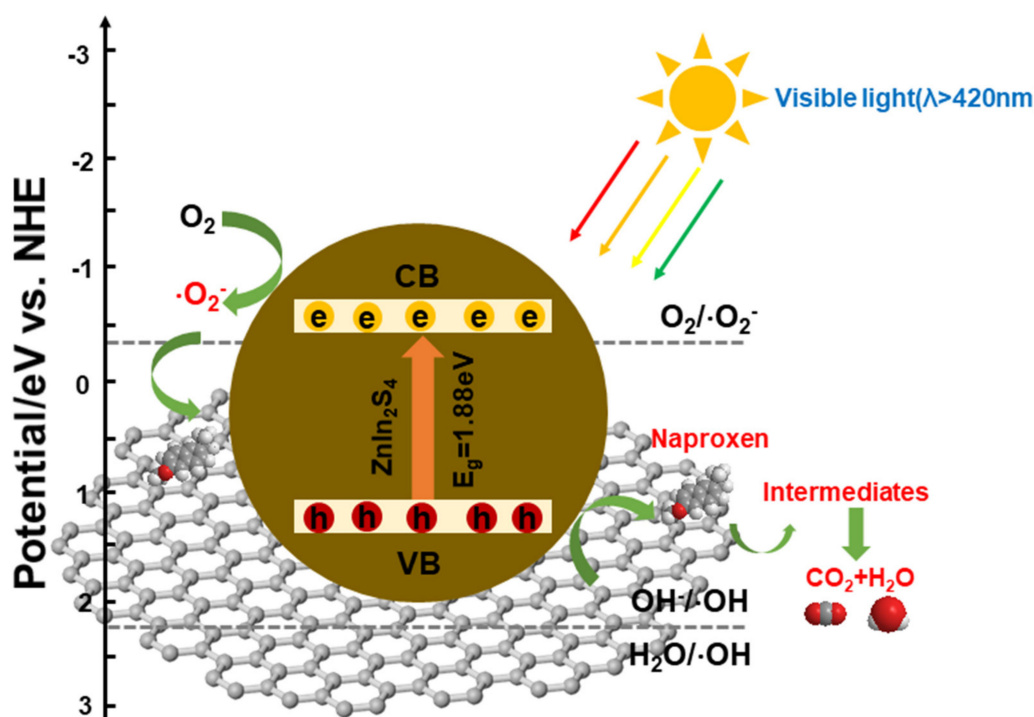


Figure 7. Schematic illustration for photogenerated carriers transfers and photocatalytic mechanism of rGO/ZIS composites under visible-light irradiation ($\lambda > 420$ nm).

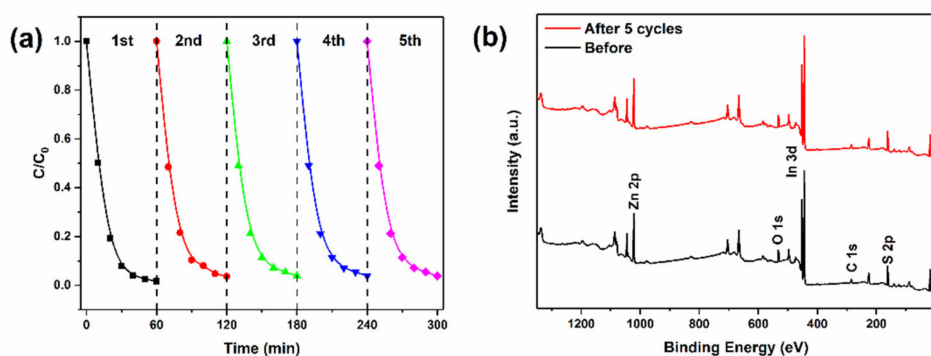


Figure 8. (a) Cycling tests for the photodegradation of NPX by rGO/ZIS-1. Reaction conditions: $[\text{NPX}] = 10 \text{ mg}\cdot\text{L}^{-1}$, $[\text{photocatalyst}] = 0.2 \text{ g}\cdot\text{L}^{-1}$, natural pH, $\lambda > 420$ nm. (b) Survey XPS spectra of rGO/ZIS-1 before and after the five cycle reactions.

2.5. Photodegradation Intermediates and Suggested Pathways

To further understand the photodegradation mechanism of NPX during the reaction process, the intermediates of NPX were analyzed by LC-MS/MS. The proposed pathway of degradation was shown in Figure 9. Seven main intermediates with m/z of 262, 216, 216, 200, 188, 170, and 358 were identified in the process of NPX photodegradation. The detection of intermediates was based on the transformation pathway of NPX degradation in the previous research literatures [4,6,31–34]. The methyl and methoxyl groups on the aromatic ring are the two sites easily attacked by reactive oxygen species [6]. After electron transfer and decarboxylation NPX was transferred to m/z 184, which was further oxidized to produce m/z 200. m/z 216 was the demethoxylation product of NPX after the methoxy group on the ring was attacked by ROS. m/z 170 and m/z 188 could be generated by the oxidation attack on the methyl position of m/z 216. m/z 262 was the hydroxylation product through the electrophilic adduct reaction [4]. In addition, m/z 358 was identified as dimeric photoproducts of m/z

188 [34], which has been detected in other work [35]. These intermediates will be further degraded into small molecules, which are finally oxidized to CO_2 and H_2O .

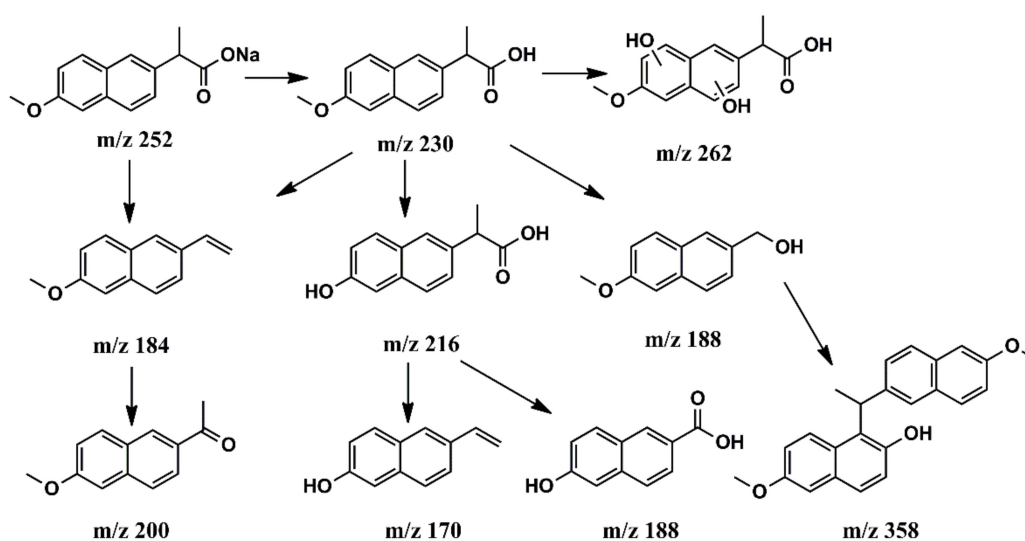


Figure 9. Proposed photodegradation pathways for NPX by rGO/ZIS-1. Reaction conditions: $[\text{NPX}] = 10 \text{ mg}\cdot\text{L}^{-1}$, $[\text{photocatalyst}] = 0.2 \text{ g}\cdot\text{L}^{-1}$, natural pH, $\lambda > 420 \text{ nm}$.

3. Materials and Methods

3.1. Materials

All chemicals and reagents were of analytical grade and used without further purification. Zinc acetate ($\text{Zn}(\text{CH}_3\text{COO})_2\cdot 2\text{H}_2\text{O}$), indium (III) nitrate hydrate ($\text{In}(\text{NO}_3)_3\cdot 4.5\text{H}_2\text{O}$), and L-cysteine were all obtained from Sinopharm Chemical Reagent Co., Ltd. (Shanghai, China). Acetonitrile (HPLC grade; $\geq 99.8\%$) was acquired from ANPEL Tech Co., Ltd. (Shanghai, China). Naproxen (NPX) was purchased from Sigma-Aldrich Chemical Co., Ltd. (St. Louis, MI, USA). Graphene oxide (GO) was sourced from XFANO Materials Tech Co., Ltd. (Jiangsu, China). Ultrapure water was produced from a Milli-Q device ($18.2 \text{ M}\Omega\cdot\text{cm}^{-1}$) and used in the all experiments.

3.2. Synthesis of Photocatalysts

Different mass ratios of reduced graphene oxide/ ZnIn_2S_4 (donated as rGO/ZIS) composites were synthesized via a hydrothermal procedure with some modification [8]. In a typical route, 0.01568 g Graphene oxide (1 wt%) and 0.2195 g (1 mmol) $\text{Zn}(\text{CH}_3\text{COO})_2\cdot 2\text{H}_2\text{O}$, 0.76384 g (2 mmol) $\text{In}(\text{NO}_3)_3\cdot 4.5\text{H}_2\text{O}$ and 0.4846 g (4 mmol) L-cysteine were firstly added into 30 mL of ultrapure water, then the mixture was magnetically stirred for 30 min and transferred into a 50 mL Teflon-lined stainless steel autoclave. Afterward, the autoclave was sealed and maintained at $180 \text{ }^\circ\text{C}$ for 12 h in an oven. Finally, the obtained 1 wt% rGO/ZIS was collected, washed with ethanol and deionized water for several times, and dried in an oven at $60 \text{ }^\circ\text{C}$ for 24 h. On this basis, different mass ratios of rGO/ZIS with loadings of 0.5 wt%, 1 wt%, 2.5 wt%, 5 wt%, and 8wt % were prepared and denoted as rGO/ZIS-0.5, rGO/ZIS-1, rGO/ZIS-2.5, rGO/ZIS-5, and rGO/ZIS-8, respectively. The pure ZnIn_2S_4 sample was prepared under the same experimental conditions without the addition of GO.

3.3. Characterization of Photocatalysts

The details of characterizations were provided in Text S1.

3.4. Photocatalytic Degradation Experiments

The photocatalytic performance was examined by the degradation of NPX under visible-light irradiation ($\lambda > 420$ nm). A 300W xenon lamp (Perfect Light, PLS-SXE300,) with a 420 nm cutoff filter was used as the light source, and the intensity of the light was 115 mW/cm^2 . In a typical experiment, 20 mg as-prepared photocatalyst were dispersed into the quartz reactors which contains 100 mL NPX aqueous solution ($10 \text{ mg}\cdot\text{L}^{-1}$, without pH adjustment). Then the quartz reactor is placed on a magnetic stirrer and the temperature was maintained at 25°C using a recirculated cooling water system. Prior to irradiation, the solution was stirred for 30 min in dark to research the adsorption/desorption equilibrium. 3 mL aliquots were collected at the given time intervals and filtrated through $0.22 \mu\text{m}$ PES syringe filters to remove the photocatalyst. Finally, the filtrates were tested by HPLC.

3.5. Analytical Methods

The concentrations of NPX were measured by a reversed-phase high-performance liquid chromatography system (Aglient1200, CA, USA). Equipped with a UV detector and a Synchronis column (4.6×250 mm, $5 \mu\text{m}$ particle size, Thermo Fisher Scientific Inc., Waltham, MA, USA). Acetonitrile and water were used as the mobile phase (65:35, *v/v*) at a flow rate of $1 \text{ mL}\cdot\text{min}^{-1}$. The column temperature was maintained at 30°C and the detection wavelength was set at 240 nm. The degradation intermediates were detected by LC-MS/MS (Thermo Fisher Scientific TSQ Quantum, Waltham, MA, USA) during the photocatalytic degradation process and more details of analysis can be found in Text S2.

4. Conclusions

We have successfully prepared nanocomposite photocatalyst reduced graphene oxide/ ZnIn_2S_4 (rGO/ZIS) via a simple one-step hydrothermal method. rGO/ZIS shown superior photocatalytic degradation activity in contrast to the pure ZnIn_2S_4 under visible light. The results of photoelectric characterization demonstrated that the higher charge carrier mobility and expansion of absorption range of light are responsible for the improvement of photocatalytic performance. Furthermore, reactive species trapping experiments and EPR signals proved that superoxide radical ($\bullet\text{O}_2^-$) and hole (h^+) are the main reactive species in the photocatalytic degradation reaction. Finally, seven degradation byproducts were identified and the possible degradation route was proposed based on the LC-MS/MS results. We hope that this work can provide some insights for the design and application of ternary chalcogenide semiconductor composites in the field of photocatalytic environmental remediation.

Supplementary Materials: The following are available online at <http://www.mdpi.com/2073-4344/10/6/710/s1>, Figure S1: High-resolution XPS spectra of C 1s in GO, Figure S2: Nitrogen adsorption-desorption isotherms (a) and corresponding pore size distribution(b), Figure S3: The Zeta potential of 1% rGO/ZIS in different solution pH at 25°C , Figure S4: (a) photocatalytic degradation of DCF with different photocatalysts and (b) plots of $-\ln(\text{C}/\text{C}_0)$ vs irradiation time. Reaction conditions: $[\text{DCF}] = 10 \text{ mg}\cdot\text{L}^{-1}$, $[\text{photocatalyst}] = 0.2 \text{ g}\cdot\text{L}^{-1}$, natural pH, $\lambda > 420$ nm, Table S1: BET experimental results of GO, ZnIn_2S_4 and rGO/ ZnIn_2S_4 .

Author Contributions: Data curation, K.F.; Funding acquisition, H.D.; Investigation, C.D. and J.S.; Methodology, Y.P. and J.S.; Project administration, J.S. and H.D. All authors have read and agreed to the published version of the manuscript.

Funding: This research was funded by the Major Science and Technology Program for Water Pollution Control and Treatment (grant number. 2017ZX07201003 and 2017ZX07501001), China.

Conflicts of Interest: The authors declare no conflict of interest.

References

1. Liang, R.; Luo, S.; Jing, F.; Shen, L.; Qin, N.; Wu, L. A simple strategy for fabrication of Pd@MIL-100(Fe) nanocomposite as a visible-light-driven photocatalyst for the treatment of pharmaceuticals and personal care products (PPCPs). *Appl. Catal. B* **2015**, *176–177*, 240–248. [[CrossRef](#)]

2. Kumar, A.; Khan, M.; Fang, L.; Lo, I.M.C. Visible-light-driven N-TiO₂@SiO₂@Fe₃O₄ magnetic nanophotocatalysts: Synthesis, characterization, and photocatalytic degradation of PPCPs. *J. Hazard Mater.* **2019**, *370*, 108–116. [[CrossRef](#)] [[PubMed](#)]
3. Ray, S.K.; Dhakal, D.; Lee, S.W. Rapid degradation of naproxen by AgBr- α -NiMoO₄ composite photocatalyst in visible light: Mechanism and pathways. *Chem. Eng. J.* **2018**, *347*, 836–848. [[CrossRef](#)]
4. Wang, F.; Wang, Y.; Feng, Y.; Zeng, Y.; Xie, Z.; Zhang, Q.; Su, Y.; Chen, P.; Liu, Y.; Yao, K.; et al. Novel ternary photocatalyst of single atom-dispersed silver and carbon quantum dots co-loaded with ultrathin g-C₃N₄ for broad spectrum photocatalytic degradation of naproxen. *Appl. Catal. B* **2018**, *221*, 510–520. [[CrossRef](#)]
5. Begum, S.; Ahmaruzzaman, M. Biogenic synthesis of SnO₂/activated carbon nanocomposite and its application as photocatalyst in the degradation of naproxen. *Appl. Surf. Sci.* **2018**, *449*, 780–789. [[CrossRef](#)]
6. Chi, H.; He, X.; Zhang, J.; Wang, D.; Zhai, X.; Ma, J. Hydroxylamine enhanced degradation of naproxen in Cu²⁺ activated peroxymonosulfate system at acidic condition: Efficiency, mechanisms and pathway. *Chem. Eng. J.* **2019**, *361*, 764–772. [[CrossRef](#)]
7. Chi, H.; Wang, Z.; He, X.; Zhang, J.; Wang, D.; Ma, J. Activation of peroxymonosulfate system by copper-based catalyst for degradation of naproxen: Mechanisms and pathways. *Chemosphere* **2019**, *228*, 54–64. [[CrossRef](#)]
8. Guo, F.; Cai, Y.; Guan, W.; Huang, H.; Liu, Y. Graphite carbon nitride/ZnIn₂S₄ heterojunction photocatalyst with enhanced photocatalytic performance for degradation of tetracycline under visible light irradiation. *J. Phys. Chem. Solids* **2017**, *110*, 370–378. [[CrossRef](#)]
9. Wang, S.; Guan, B.Y.; Wang, X.; Lou, X.W.D. Formation of Hierarchical Co₉S₈@ZnIn₂S₄ Heterostructured Cages as an Efficient Photocatalyst for Hydrogen Evolution. *J. Am. Chem. Soc.* **2018**, *140*, 15145–15148. [[CrossRef](#)]
10. Gou, X.L.; Cheng, F.Y.; Shi, Y.H.; Zhang, L.; Peng, S.J.; Chen, J.; Shen, P.W. Shape-controlled synthesis of ternary chalcogenide ZnIn₂S₄ and CuIn(S,Se)₂ nano-/microstructures via facile solution route. *J. Am. Chem. Soc.* **2006**, *128*, 7222–7229. [[CrossRef](#)]
11. Tian, Q.; Wu, W.; Liu, J.; Wu, Z.; Yao, W.; Ding, J.; Jiang, C. Dimensional heterostructures of 1D CdS/2D ZnIn₂S₄ composited with 2D graphene: Designed synthesis and superior photocatalytic performance. *Dalton Trans.* **2017**, *46*, 2770–2777. [[CrossRef](#)]
12. Qiu, P.; Yao, J.; Chen, H.; Jiang, F.; Xie, X. Enhanced visible-light photocatalytic decomposition of 2,4-dichlorophenoxyacetic acid over ZnIn₂S₄/g-C₃N₄ photocatalyst. *J. Hazard Mater.* **2016**, *317*, 158–168. [[CrossRef](#)] [[PubMed](#)]
13. Zhang, S.; Wang, L.; Liu, C.; Luo, J.; Crittenden, J.; Liu, X.; Cai, T.; Yuan, J.; Pei, Y.; Liu, Y. Photocatalytic wastewater purification with simultaneous hydrogen production using MoS₂ QD-decorated hierarchical assembly of ZnIn₂S₄ on reduced graphene oxide photocatalyst. *Water Res.* **2017**, *121*, 11–19. [[CrossRef](#)] [[PubMed](#)]
14. Zhu, T.; Ye, X.; Zhang, Q.; Hui, Z.; Wang, X.; Chen, S. Efficient utilization of photogenerated electrons and holes for photocatalytic redox reactions using visible light-driven Au/ZnIn₂S₄ hybrid. *J. Hazard Mater.* **2019**, *367*, 277–285. [[CrossRef](#)] [[PubMed](#)]
15. Yan, A.; Shi, X.; Huang, F.; Fujitsuka, M.; Majima, T. Efficient photocatalytic H₂ evolution using NiS/ZnIn₂S₄ heterostructures with enhanced charge separation and interfacial charge transfer. *Appl. Catal. B* **2019**, *250*, 163–170. [[CrossRef](#)]
16. Lim, W.Y.; Hong, M.; Ho, G.W. In situ photo-assisted deposition and photocatalysis of ZnIn₂S₄/transition metal chalcogenides for enhanced degradation and hydrogen evolution under visible light. *Dalton Trans.* **2016**, *45*, 552–560. [[CrossRef](#)]
17. Jiao, X.; Chen, Z.; Li, X.; Sun, Y.; Gao, S.; Yan, W.; Wang, C.; Zhang, Q.; Lin, Y.; Luo, Y.; et al. Defect-Mediated Electron-Hole Separation in One-Unit-Cell ZnIn₂S₄ Layers for Boosted Solar-Driven CO₂ Reduction. *J. Am. Chem. Soc.* **2017**, *139*, 7586–7594. [[CrossRef](#)]
18. Ye, L.; Fu, J.; Xu, Z.; Yuan, R.; Li, Z. Facile one-pot solvothermal method to synthesize sheet-on-sheet reduced graphene oxide (RGO)/ZnIn₂S₄ nanocomposites with superior photocatalytic performance. *ACS Appl. Mater. Interfaces* **2014**, *6*, 3483–3490. [[CrossRef](#)]
19. Che, W.; Luo, Y.; Deng, F.; Zhang, A.; Zhao, L.; Luo, X.; Ruan, Q. Facile solvothermal fabrication of cubic-like reduced graphene oxide/AgIn₅S₈ nanocomposites with anti-photocorrosion and high visible-light photocatalytic performance for highly-efficient treatment of nitrophenols and real pharmaceutical wastewater. *Appl. Catal. A Gen.* **2018**, *565*, 170–180. [[CrossRef](#)]

20. Wang, J.; Tsuzuki, T.; Tang, B.; Hou, X.; Sun, L.; Wang, X. Reduced graphene oxide/ZnO composite: Reusable adsorbent for pollutant management. *ACS Appl. Mater. Interfaces* **2012**, *4*, 3084–3090. [[CrossRef](#)]
21. Xie, C.; Lu, X.; Deng, F.; Luo, X.; Gao, J.; Dionysiou, D.D. Unique surface structure of nano-sized CuInS₂ anchored on rGO thin film and its superior photocatalytic activity in real wastewater treatment. *Chem. Eng. J.* **2018**, *338*, 591–598. [[CrossRef](#)]
22. Li, H.; Yu, H.; Chen, S.; Zhao, H.; Zhang, Y.; Quan, X. Fabrication of graphene wrapped ZnIn₂S₄ microspheres heterojunction with enhanced interfacial contact and its improved photocatalytic performance. *Dalton Trans.* **2014**, *43*, 2888–2894. [[CrossRef](#)] [[PubMed](#)]
23. Jeevitha, G.; Abhinayaa, R.; Mangalaraj, D.; Ponpandian, N. Tungsten oxide-graphene oxide (WO₃-GO) nanocomposite as an efficient photocatalyst, antibacterial and anticancer agent. *J. Phys. Chem. Solids* **2018**, *116*, 137–147. [[CrossRef](#)]
24. Wang, H.; Zhang, M.; He, X.; Du, T.; Wang, Y.; Li, Y.; Hao, T. Facile prepared ball-like TiO₂ at GO composites for oxytetracycline removal under solar and visible lights. *Water Res.* **2019**, *160*, 197–205. [[CrossRef](#)] [[PubMed](#)]
25. Khazaei, Z.; Mahjoub, A.R.; Cheshme Khavar, A.H.; Srivastava, V.; Sillanpää, M. Synthesis of layered perovskite Ag₂F-Bi₂MoO₆/rGO: A surface plasmon resonance and oxygen vacancy promoted nanocomposite as a visible-light photocatalyst. *J. Photochem. Photobiol. A Chem.* **2019**, *379*, 130–143. [[CrossRef](#)]
26. Zhang, S.; Liu, X.; Liu, C.; Luo, S.; Wang, L.; Cai, T.; Zeng, Y.; Yuan, J.; Dong, W.; Pei, Y.; et al. MoS₂ Quantum Dot Growth Induced by S Vacancies in a ZnIn₂S₄ Monolayer: Atomic-Level Heterostructure for Photocatalytic Hydrogen Production. *ACS Nano* **2018**, *12*, 751–758. [[CrossRef](#)]
27. Tien, H.N.; Luan, V.H.; Hoa, L.T.; Khoa, N.T.; Hahn, S.H.; Chung, J.S.; Shin, E.W.; Hur, S.H. One-pot synthesis of a reduced graphene oxide–zinc oxide sphere composite and its use as a visible light photocatalyst. *Chem. Eng. J.* **2013**, *229*, 126–133. [[CrossRef](#)]
28. Yan, T.; Yan, Q.; Wang, X.; Liu, H.; Li, M.; Lu, S.; Xu, W.; Sun, M. Facile fabrication of heterostructured g-C₃N₄/Bi₂MoO₆ microspheres with highly efficient activity under visible light irradiation. *Dalton Trans.* **2015**, *44*, 1601–1611. [[CrossRef](#)]
29. Miao, X.; Ji, Z.; Wu, J.; Shen, X.; Wang, J.; Kong, L.; Liu, M.; Song, C. g-C₃N₄/AgBr nanocomposite decorated with carbon dots as a highly efficient visible-light-driven photocatalyst. *J. Colloid. Interface Sci.* **2017**, *502*, 24–32. [[CrossRef](#)]
30. Chen, F.; Li, D.; Luo, B.; Chen, M.; Shi, W. Two-dimensional heterojunction photocatalysts constructed by graphite-like C₃N₄ and Bi₂WO₆ nanosheets: Enhanced photocatalytic activities for water purification. *J. Alloys Compd.* **2017**, *694*, 193–200. [[CrossRef](#)]
31. Dulova, N.; Kattel, E.; Trapido, M. Degradation of naproxen by ferrous ion-activated hydrogen peroxide, persulfate and combined hydrogen peroxide/persulfate processes: The effect of citric acid addition. *Chem. Eng. J.* **2017**, *318*, 254–263. [[CrossRef](#)]
32. Arany, E.; Szabo, R.K.; Apati, L.; Alapi, T.; Ilisz, I.; Mazellier, P.; Dombi, A.; Gajda-Schranz, K. Degradation of naproxen by UV, VUV photolysis and their combination. *J. Hazard Mater.* **2013**, *262*, 151–157. [[CrossRef](#)] [[PubMed](#)]
33. Gao, Y.-q.; Gao, N.-y.; Chu, W.-h.; Yang, Q.-l.; Yin, D.-q. Kinetics and mechanistic investigation into the degradation of naproxen by a UV/chlorine process. *RSC Adv.* **2017**, *7*, 33627–33634. [[CrossRef](#)]
34. Kanakaraju, D.; Motti, C.A.; Glass, B.D.; Oelgemoller, M. TiO₂ photocatalysis of naproxen: Effect of the water matrix, anions and diclofenac on degradation rates. *Chemosphere* **2015**, *139*, 579–588. [[CrossRef](#)] [[PubMed](#)]
35. DellaGreca, M.; Brigante, M.; Isidori, M.; Nardelli, A.; Previtera, L.; Rubino, M.; Temussi, F. Phototransformation and ecotoxicity of the drug Naproxen-Na. *Environ. Chem. Lett.* **2003**, *1*, 237–241. [[CrossRef](#)]

